Wide-Band Electromagnetic Wave Propagation and Resonance in Long Cobalt Nanoprisms

M.M. Aziz[1,*] and C. McKeever[2]

[1] *Department of Engineering, University of Exeter, Exeter EX4 4QF, United Kingdom*
[2] *Department of Physics, University of Exeter, Exeter EX4 4QL, United Kingdom*

(Received 2 December 2019; revised manuscript received 29 December 2019; accepted 4 March 2020; published 30 March 2020)

Electromagnetic wave interaction with confined metallic magnetic structures is complex due to the excitation of nonuniform electromagnetic fields and magnetic precession and spin-wave modes over length scales that are dependent on the geometric, electromagnetic, and micromagnetic properties of the magnetic structures. Here, we solve the coupled system of Maxwell's equations and the Landau-Lifshitz-Gilbert equation using a stable algorithm based on the finite-difference time-domain method to study the transient wide-band electromagnetic propagation and resonance in infinitely long cobalt nanoprisms with a square cross section of side lengths 50–1000 nm. In particular, we identify the resonance mechanisms through studying the local transient and spectral distributions of magnetization in the prisms. The nanoprisms are excited by an axially polarized plane wave at normal incidence with a 70 GHz Gaussian pulse profile. For this incident wave condition, the simulations confirm that resonance in the cobalt prisms is excited mainly by the current-induced magnetic fields and indicate a magnetization curling resonance mode for prism side lengths less than 100 nm. The eigenfrequencies for the curling mode are confirmed theoretically using a model for an equivalent long circular cylinder with radial spin-wave modes. For prism side lengths longer than 100 nm (but less than the nonmagnetic skin depth), the magnetic response is confined to thin regions along the prism edges due to resonance-induced skin effects. The simulations indicate predominately uniform magnetization precession in the confined edge regions with increased pinning in the corners. The uniform resonance mode in the central part of the edge regions increases in intensity with prism size, with frequency described using Kittel's ferromagnetic resonance frequency of a thin planar structure. A higher-frequency size-independent uniform resonance mode is observed in the corner regions with frequency determined by the local demagnetizing factors. Local and integrated power absorption spectra are calculated using the simulated transient magnetization and fields, and confirm the resonance modes and frequencies in the cobalt prisms and their size dependence. The profile of the local power absorption spectra is also used to estimate the thickness of the confined edge regions or magnetic skin depth in the cobalt prisms at the fundamental resonance mode and is found to be approximately 50 nm. The outcomes of this work would benefit the design and engineering of lightweight and compact materials and devices incorporating metallic magnetic nanostructures. This work also provides a foundation for further modeling and understanding of electromagnetic transmission and propagation in more complex metallic ferromagnetic structures and composites excited by different electromagnetic wave conditions.

DOI: 10.1103/PhysRevApplied.13.034073

I. INTRODUCTION

There is strong interest in understanding the magnetization dynamics and resonance mechanism in confined metallic ferromagnetic nanostructures and their alloys for various applications. Further to the ability of configuring their magnetic response by controlling their shape, size, microstructure, and bias field, they also offer higher magnetic moments compared with ferrites. This results in enhanced resonance frequencies, and hence, operating bandwidths for microwave devices and metamaterials [1–4]. The enhanced bandwidth is also of particular interest to electromagnetic wave interaction with conductive ferromagnetic structures and composites for applications in telecommunications and wave absorption [5–7] and for noise suppression [8]. Metallic ferromagnets and alloys are also compatible with CMOS fabrication methods, which makes them attractive for the development of practicable spintronic and magnonic nanostructures and devices [9–12].

Electromagnetic wave interaction with conductive confined magnetic structures, which is the focus of this article, complicates magnetization dynamics due to the excitation of strongly coupled nonuniform electromagnetic fields and

*m.m.aziz@ex.ac.uk

 © 2020 American Physical Society

magnetization, with local dispersive permeabilities and damping. These will affect wave transmission through the magnetic structure over different length scales (or skin depths), and hence, influence the resonance mechanism and frequencies. Combining both electromagnetic wave propagation and micromagnetics of ferromagnetic metallic structures complicates the theoretical development and interpretation of ferromagnetic resonance measurements, which depend on the magnetization configuration and excited resonance modes.

Earlier theoretical studies of ferromagnetic resonance (FMR) in confined structures, excited only by magnetic fields, focused on cylinders with large axial to radial dimensions (whiskers or nanowires). This interest in cylindrical structures stems from the ability to configure their magnetic response through control of their geometry, size, and anisotropy [13] and equally to simplify the theoretical treatment of both the micromagnetics and magnetostatics resulting from the natural two-dimensional symmetry in the cylindrical structure. This includes Kittel's well-known FMR frequency expressions for uniform precession from the solution of the linearized Landau-Lifshitz-Gilbert (LLG) torque equation considering only the magnetostatic field contribution [14]. Neglecting exchange interactions, Joseph and Schlömann [15] also derived the dipolar eigenfrequencies for nonuniform precession modes (surface and volume) in long cylinders, indicating a decrease in resonance frequency with a reduction in magnetostatic wavelengths. In the absence of magnetostatics and considering only exchange interactions, Brown [16], on the other hand, derived the eigenfrequencies for magnetization curling in an infinite circular cylinder above a critical radius, where the total energy was reduced. Arias and Mills [17] extended the linear theory to include both magnetostatic and exchange contributions to numerically determine the resonance eigenvalues and used quasistatic vector potential formulation to model eddy current effects in conductive magnetic cylinders. However, and due to the complexity of the solution in the dipolar-exchange system, their theoretical development did not yield the local dynamic magnetization distribution and the size dependence of the resonance modes, nor the effects of electromagnetic wave propagation and power absorption.

Appropriate treatment of electromagnetic wave interaction with conductive magnetic nanostructures requires the simultaneous solution of Maxwell's equations for electric and magnetic fields and the LLG equation of magnetization motion. The bulk of theoretical work in the literature has focused on saturated magnetic structures for simplicity and solving the coupled system of Maxwell's equations and the LLG equation, assuming wavelike harmonic solutions for the magnetization and fields, for the effective complex permeability and propagation wave vectors subject to electromagnetic and micromagnetic boundary conditions for simple geometries [4,14,18–24]. The field solutions are then used to estimate the surface impedance and power absorption for correlation and interpretation of experimental measurements. For a semi-infinite magnetic structure, Ament and Rado [18] theoretically revealed coupled electromagnetic and exchange spin waves propagating through the magnetic structure, yielding local effective permeability and surface impedance. The increase in imaginary local permeability and wave vectors at resonance leads to attenuation of propagating waves over length scales that are much smaller than the nonmagnetic skin depth [20]. The same theoretical approach was extended by Hartwell [21] to thin-film structures and highlighted the importance of surface pinning and other magnetic boundary conditions on the standing-wave resonance modes and power absorption spectra [25]. In more confined structures, Heinrich [22] indicated theoretically a dependence of the surface impedance on the radius of a long metallic magnetic wire excited by current-induced circumferential fields. Kraus *et al.* [23,24] carried out a detailed derivation of the resonance modes in a long saturated circular cylinder. They explained the size dependence of the surface impedance by the excitation of circumferential and uniform resonance modes (coupled either to the electric or magnetic fields of the incident plane wave) and the extent of the corresponding absorption lengths relative to the cylinder radius. The same simplified theoretical approach of the time harmonic solution of Maxwell's equations and the LLG equation in the linear regime was also used to investigate the relevant magnetoimpedance effects and resonance in conductive cylindrical wires, where circumferential resonance modes were mainly excited by high-frequency axial applied currents [26]. The outlined analytical and semianalytical work based on harmonic analysis, however, did not explicitly calculate the local dynamic magnetization nor local power absorption spectra to clearly identify the resonance mechanisms, study higher-frequency spin-wave modes, and to estimate explicitly the magnetic skin depth from the absorption spectra in the presence of exchange interactions at resonance. Furthermore, the wire diameter range over which the proposed resonance modes (and other higher-order exchange modes) are applicable is still ambiguous, with only the nonmagnetic skin depth used as an indicator [24], which spans hundreds of nanometers for metallic ferromagnets, even at high excitation frequencies.

Due to the complexity of modeling the wave-magnetic matter interaction, the previously outlined semianalytical work assumed simple saturated magnetic geometries, excited in the linear regime with uniform fields, and focused on the sinusoidal response, rather than the (wideband) transient response with only certain incident wave polarization. Fabricated confined two-dimensional and three-dimensional magnetic structures found, for example, in composites and metamaterials are not saturated, can have complex ground states and magnetic pinning [27],

and can be multilayered with dielectric layers or inclusions [20]. Moreover, fabricated ferromagnetic nanowires are not ideally cylindrical, but rather have edges and corners (for example, Ref. [28]). This can lead to local inhomogeneities in both electric and magnetic fields, and hence, in magnetic configuration, with different induced skin depths that alter the energy landscape and affect the resonance modes and frequencies, which cannot be captured using the existing simplified theories. There is thus the need for a deeper understanding of the wide-band electromagnetic wave propagation and power absorption in confined metallic magnetic nanostructures, to identify the resonance mechanisms and frequencies resulting from coupling with the electromagnetic fields and their dependence on the size and shape of the magnetic structures. This understanding would benefit the design and tuning of lightweight more-compact metallic magnetic structures with enhanced resonance frequencies and low electrical losses. Here, a coupled electromagnetic-micromagnetic numerical solver is used to simulate the transient wide-band magnetic response in infinitely long conductive cobalt prisms with square cross sections of side lengths 50–1000 nm, excited by a 70 GHz Gaussian electromagnetic plane wave. The focus here will be on studying the local distribution of the transient magnetization and power absorption spectra to identify the resonance mechanisms and frequencies in the prisms and their size dependence.

The approach used here to model and simulate the transient electromagnetic wave interaction with cobalt prisms is by integrating the Landau-Lifshitz-Gilbert equation within the finite-difference time-domain (FDTD) Maxwell's equations solver. The FDTD method, through its structure and implementation, provides a flexible framework for the simulation of a wide range of electromagnetic phenomena, providing almost infinite bandwidth due to its time domain nature [29]. This combined electromagnetic-micromagnetic approach, hereafter referred to as the FDTD-LLG method, allows computation of the dynamic behavior of the magnetic moments in a magnetic material subject to various micromagnetic energies (anisotropy, exchange, and external fields). This is while naturally evaluating the transient magnetic fields inside and outside the material from the induced magnetic charges and currents through Maxwell's equations. Thus, the FDTD-LLG approach has been gaining increased attention for modeling and simulation of conductive magnetic structures [30], including studying the broadband ferromagnetic resonance of thin-film magnetic nanostructures with nonmagnetic metallic layers [31], the impact of eddy currents on the dispersion of magnetostatic surface waves in thin conducting films [32], the nonlinear magnetic response in thin-film rf devices [33], and for modeling and simulating high-power microwave devices [34,35]. The success of this approach is dependent on the ability to provide an appropriate spatial discretization scheme and a corresponding stable time-marching algorithm for the integration of the LLG equation within the Maxwell's equation solver. Previous work incorporating the LLG equation within the FDTD method was limited to linearized forms of the LLG equation, which did not include magnetocrystalline anisotropy and exchange coupling, without appropriate treatment of magnetic boundary conditions, and used explicit time-marching schemes that were unstable for small damping [36–40]. Furthermore, four-point and less-accurate spatial interpolations were required to evaluate the magnetization at the staggered field locations within the FDTD grid [36,37,39,40]. The complete form of the LLG equation was included in a stable FDTD implementation including anisotropy and exchange [41], but used a numerically dispersive unstaggered FDTD grid for the implementation. An efficient and stable implementation was developed by Aziz [42] that integrated the complete form of the LLG equation (including anisotropy and exchange) within the FDTD method. In this implementation, a numerically efficient discretization scheme was used to locate the magnetization vectors at the corners of the FDTD cell to allow simple two-point interpolations to evaluate the magnetization at the staggered field locations without numerical dispersion. This stable algorithm and magnetic grid discretization approach for the FDTD-LLG method will be used here and adapted to simulate the electromagnetic wave propagation and magnetic resonance in the cobalt prisms.

Section II provides the mathematical description of Maxwell's equations and the LLG equation used in the numerical implementation. Section III describes the FDTD space and time discretization schemes and unit cell, absorbing boundary conditions, and plane-wave source conditions. The discretization scheme of the magnetization in the LLG equation and stable time-marching algorithm are also detailed in Sec. III. The simulation results are presented in Sec. V along with analysis of the computed dynamic magnetization and power absorption spectra. SI units are used throughout this article.

II. MATHEMATICAL MODELS

A. Maxwell's equations

For a lossy and dispersive medium, Maxwell's curl equations are given by

$$\frac{\partial \mathbf{B}}{\partial t} = -\nabla \times \mathbf{E}, \tag{1}$$

$$\varepsilon \frac{\partial \mathbf{E}}{\partial t} = \nabla \times \mathbf{H} - \sigma \mathbf{E}, \tag{2}$$

where $\mathbf{H}$ is the magnetic field, $\mathbf{E}$ is the electric field, ε is the permittivity, σ is the electrical conductivity, and t is the time. The magnetic flux density $\mathbf{B}$ is related to the magnetization in a magnetic medium through the constitutive

relation:

$$\mathbf{B} = \mu_0(\mathbf{M} + \mathbf{H}), \tag{3}$$

where μ_0 is the permeability of free space.

The focus in this article is on the transverse-magnetic (TMz) mode for simplicity, where the fields and magnetization are assumed to be spatially invariant over the long axis of the cobalt prisms. This mode also accounts for the induced axial currents in the prisms due to the z-polarized incident plane wave. Nevertheless, the numerical implementation presented here is applicable to the full three-dimensional Maxwell's equations. In the TMz mode, Maxwell's curl equations reduce to

$$\frac{\partial B_x}{\partial t} = -\frac{\partial E_z}{\partial y}, \tag{4}$$

$$\frac{\partial B_y}{\partial t} = \frac{\partial E_z}{\partial x}, \tag{5}$$

$$\varepsilon\frac{\partial E_z}{\partial t} = \frac{\partial H_y}{\partial x} - \frac{\partial H_x}{\partial y} - \sigma E_z. \tag{6}$$

B. The Landau-Lifshitz-Gilbert equation

The Landau-Lifshitz equation with the Gilbert damping term (LLG) is used in this work to model the dynamic magnetization in response to an effective torque field $\mathbf{H}_{\text{eff}}$ and is given by [16]

$$\frac{d\mathbf{M}}{dt} = -|\gamma|[\mathbf{M}\times\mathbf{H}_{\text{eff}}(\mathbf{M})] + \frac{\alpha}{|\mathbf{M}|}\left(\mathbf{M}\times\frac{d\mathbf{M}}{dt}\right), \tag{7}$$

where $\gamma = 1.75882\times10^{11}\mu_0$ (m·Hz/A) is the gyromagnetic ratio, α is the phenomenological Gilbert damping coefficient, and $|\mathbf{M}| = M_s$ is the saturation magnetization. The gyromagnetic ratio here corresponds to a Landé g factor $g = 2$ for spin motion, which is within the experimentally measured values for Co [43]. The small deviations due to orbital contributions will not change the outcomes and conclusions of this work and only lead to small shifts in the calculated resonance frequencies. The effective field in Eq. (7) is given by

$$\mathbf{H}_{\text{eff}}(\mathbf{M}) = \mathbf{H}_{\text{app}} + \mathbf{H}(\mathbf{M}) + \mathbf{H}_k(\mathbf{M}) + \mathbf{H}_{\text{ex}}(\mathbf{M}), \tag{8}$$

which includes the contribution of the following fields:

1. Applied field, H_{app}

This is the internal field specified by the user inside the magnetic structure and can be static or transient, uniform or nonuniform. This field contribution is used here to specify the uniform static bias field along the prism axis.

2. Maxwell field, H

The Maxwell fields are computed from the direct solution of the transient Maxwell's equations described in Eqs. (1) and (2) in the finite-difference time-domain scheme and include contributions from electric currents, magnetic charges, and incident and scattered electromagnetic waves.

3. Exchange field, H_{ex}

The exchange field provides the energy for aligning neighboring magnetic spins due to quantum mechanical forces and for nearest neighboring contributions is given by [16]

$$\mathbf{H}_{\text{ex}} = \frac{2A}{\mu_0 M_s^2}\nabla^2\mathbf{M}, \tag{9}$$

where A is the exchange constant and ∇^2 is the Laplacian operator. Solution of the LLG equation requires definition of the appropriate boundary conditions at the surfaces of the magnetic material arising from the Laplacian in the exchange field in Eq. (9). In the absence of surface anisotropy for simplicity, the generalized exchange boundary condition in Ref. [19] reduces to the unpinned magnetization boundary condition [16,19]:

$$\frac{\partial\mathbf{M}}{\partial\mathbf{n}} = 0, \tag{10}$$

where $\mathbf{n}$ is the vector normal to the surface of the magnetic material. In the absence of exchange interactions, the boundary conditions of the combined system of Maxwell's and LLG equations are naturally satisfied by the electromagnetic boundary conditions of Maxwell's curl equations.

4. Anisotropy field, H_k

Uniaxial anisotropy is used in this work to describe the hexagonal close-packed structure of the cobalt prism along the prism axis (z direction) and is given by

$$\mathbf{H}_k = \frac{dE_k}{d\mathbf{M}}, \tag{11}$$

where the anisotropy energy density E_k can be written as [44]

$$E_k = K_1\left[1 - \left(\frac{M_z}{M_s}\right)^2\right] + K_2\left[1 - \left(\frac{M_z}{M_s}\right)^2\right]^2,$$

and K_1 and K_2 are the anisotropy constants. In the TMz mode, the FDTD method includes two magnetic field components, while the LLG equation is solved for all three-vector magnetization components, which are invariant in the z direction.

III. NUMERICAL IMPLEMENTATION

A. The FDTD method

The FDTD method specifically provides an explicit second-order accurate transient solution for the complete set of Maxwell's curl equations for the electric and magnetic fields [29]. This makes this approach ideal here for simulating the wide-band interaction of electromagnetic waves (propagation, scattering, and absorption) with magnetic structures. Finite differences are also widely used in numerical micromagnetics (for example, Ref. [45]), with a wealth of knowledge to enable convenient and efficient integration of the LLG equation within the FDTD method. Fine geometrical features and curved surfaces (which are normally modeled more efficiently using finite elements) can still be handled in the FDTD method using local subcell models and nonuniform grid schemes [29].

The description of the efficient implementation of the FDTD LLG method is presented in our previous work [42]. Fundamental and relevant parts are repeated and expanded here for completeness. Figure 1 shows the FDTD grid with the basic unit cell (Yee cell) in the TMz mode [46]. In this arrangement, each **E** field component in the center of the cell is evaluated from the curl of the four surrounding magnetic field components, while each **H** field component is evaluated using the curl of the two neighboring **E** field components. The electric and magnetic fields are not colocated in space and displaced from each other by half a cell length. This field arrangement naturally enforces the electromagnetic boundary conditions of Maxwell's equations at the interfaces of different materials [29].

The convention used here to represent the discretized field component f in two dimensions is $f|_{i,j}^{n} = f(i\Delta x, j\,\Delta y; n\Delta dt)$, where subscripts i and j are integers representing spatial grid locations in the x and y directions, respectively, and superscript n is an integer representing the time-step increment Δt. For simplicity, square cells are used here with $\Delta x = \Delta y$. Second-order accurate central differences are used; for example, the spatial discretization of Eq. (4) at time-step n yields

$$\left.\frac{\partial B_x}{\partial t}\right|_{i+1/2,j}^{n} \approx -\left(\frac{E_z|_{i+1/2,j+1/2}^{n} - E_z|_{i+1/2,j-1/2}^{n}}{\Delta x}\right). \quad (12)$$

Time integration is achieved using a second-order accurate leapfrog algorithm, where the magnetic flux density **B** in Eqs. (4) and (5) is evaluated at time-step n, which is then used to evaluate electric field **E** at time-step $n+1/2$ in Eq. (6) and so forth [29]. Applying this discretization scheme and evaluating the time average of the electric field using

$$E_z|^{n+1/2} = \frac{E_z|^{n} + E_z|^{n+1}}{2},$$

produces explicit discretized update equations for the TMz field components in Eqs. (4)–(6):

$$B_x|_{i+1/2,j}^{n+1/2} = B_x|_{i+1/2,j}^{n-1/2} - \frac{\Delta t}{\Delta x}[E_z|_{i+1/2,j+1/2}^{n} - E_z|_{i+1/2,j-1/2}^{n}], \quad (13)$$

$$B_y|_{i,j+1/2}^{n+1/2} = B_y|_{i,j+1/2}^{n-1/2} + \frac{\Delta t}{\Delta x}[E_z|_{i+1/2,j+1/2}^{n} - E_z|_{i-1/2,j+1/2}^{n}], \quad (14)$$

$$E_z|_{i+1/2,j+1/2}^{n+1} = \left(\frac{1+\sigma\Delta t/(2\varepsilon)}{1-\sigma\Delta t/(2\varepsilon)}\right) E_z|_{i+1/2,j+1/2}^{n} + \frac{\Delta t}{\Delta x[1+\sigma\Delta t/(2\varepsilon)]} \times \begin{bmatrix} H_y|_{i+1,j+1/2}^{n+1/2} - H_y|_{i,j+1/2}^{n+1/2} \\ -H_x|_{i+1/2,j+1}^{n+1/2} + H_x|_{i+1/2,j}^{n+1/2} \end{bmatrix}, \quad (15)$$

where σ and ε are understood to be located in space at the same point as their respective field components. The magnetic field **H** in Eq. (15) is computed from Eqs. (13) and (14) using the constitutive relation in Eq. (3)

$$\mathbf{H}^{n+1/2} = \frac{\mathbf{B}^{n+1/2}}{\mu_0} - \mathbf{M}^{n+1/2} \text{ inside magnetic material}$$

$$\mathbf{H}^{n+1/2} = \frac{\mathbf{B}^{n+1/2}}{\mu_0\mu_r} \text{ outside magnetic material}, \quad (16)$$

where μ_r is the relative permeability.

Evaluation of the magnetic fields in Eq. (16) and of the effective field in the LLG equation in Eq. (7) require **M** to be colocated in space with **H** and **B**, which are displaced by half-cell lengths in the FDTD grid. An efficient and simple method for the spatial discretization of the LLG equation into the staggered FDTD grid involves positioning **M** at the corners of the Yee cell, as indicated in Fig. 1 [42]. This approach requires only simple and more accurate two-point spatial interpolations to determine magnetization at

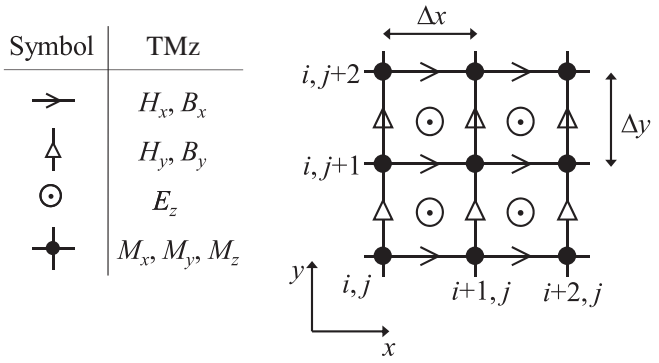

FIG. 1. Two-dimensional unit cell in the FDTD Tmz grid and efficient implementation of the finite-difference magnetization grid at the cell corners.

the magnetic field locations in the FDTD grid and clearly identifies the magnetic material boundaries. For example, the following simple two-point interpolation can be used to determine M_x at the same location as H_x or $B_x(i+1/2,j)$ in Eq. (16):

$$M_x|_{i+1/2,j}^{n+1/2} = \frac{M_x|_{i+1,j}^{n+1/2} + M_x|_{i,j}^{n+1/2}}{2}.$$

Similar interpolations are carried out to evaluate the remaining magnetization components at the magnetic field locations in the FDTD update equations. This approach can also be applied to three-dimensional grids.

The FDTD LLG simulations are excited with a transverse electromagnetic plane wave introduced using a four-cell-wide total-field scattered-field (TFSF) boundary surrounding the simulation space [29]. The one-dimensional y-directed z-polarized electromagnetic plane wave is described by

$$\frac{\partial H_x}{\partial t} = \frac{-1}{\mu_0\mu_r}\frac{\partial E_z}{\partial y},$$

$$\frac{\partial E_z}{\partial t} = \frac{-1}{\varepsilon_0\varepsilon_r}\frac{\partial H_x}{\partial y},$$

which is discretized in an auxiliary one-dimensional FDTD grid and excited with the following Gaussian hard source within the scattered-field region of the TFSF boundary:

$$H_x^s = H_0 e^{-(t-t_0)^2/\tau^2}. \tag{17}$$

The timeτ describes the width of the Gaussian source at e^{-1} of its maximum amplitude H_0. The delay time t_0 specifies the shift in the center of the Gaussian function from the beginning of the simulation and is set to $t_0 = 3\tau$ to provide a smooth increase of the electromagnetic fields from their zero initial values in the simulation for stable time marching. This plane wave is introduced at the lower interface of the TFSF boundary and removed at the top of the TFSF boundary. The one-dimensional plane wave is terminated using a second-order one-direction wave equation analytical absorbing boundary condition [47], to sufficiently reduce the reflections at time steps less than the Courant limit employed in the TMz calculations.

The simulation space, including the TFSF boundary layer, are terminated with a perfectly matched layer (PML) to absorb outgoing waves and minimize reflections. The PML is implemented using Berenger's split-field formulation [48], with a third-order polynomial grading for the magnetic conductivity and 10^{-8} reflection error [29]. The number of PML cells and separation of the PML layer from the scatterer are adjusted according to the FDTD cell size, with a minimum of 20 cells for the PML layer to minimize reflection from the inner and outer PML boundaries.

B. FDTD-LLG solution algorithm

The time derivatives in the LLG equation in Eq. (7) at time-step n may be approximated using central differences as

$$\frac{\mathbf{M}^{n+1/2} - \mathbf{M}^{n-1/2}}{\Delta t} = -|\gamma|[\mathbf{M}^n \times \mathbf{H}_{\text{eff}}^n(\mathbf{M}^n)] + \frac{\alpha}{M_s}\left(\mathbf{M}^n \times \frac{\mathbf{M}^{n+1/2} - \mathbf{M}^{n-1/2}}{\Delta t}\right).$$

Rewriting the time derivative term on the right-hand-side as

$$\frac{\mathbf{M}^{n+1/2} - \mathbf{M}^{n-1/2}}{\Delta t} = \frac{(\mathbf{M}^{n+1/2} + \mathbf{M}^{n-1/2}) - 2\mathbf{M}^{n-1/2}}{\Delta t},$$

and expressing the magnetization at time-step n using the average

$$\mathbf{M}^n = \frac{\mathbf{M}^{n+1/2} + \mathbf{M}^{n-1/2}}{2},$$

yields a second-order accurate update equation for the magnetization at time-step n

$$\mathbf{M}^n = \mathbf{M}^{n-1/2} - \mathbf{M}^n \times \left[\frac{|\gamma|\Delta t}{2}\mathbf{H}_{\text{eff}}^n(\mathbf{M}^n) + \frac{\alpha}{M_s}\mathbf{M}^{n-1/2}\right], \tag{18}$$

where the effective field $\mathbf{H}_{\text{eff}}$ is defined in Eq. (8).

Equation (18) is an implicit equation, since the evaluation of the effective field requires M^n on the right-hand-side, which is not available. Moreover, the system of Maxwell and LLG equations is not linear and the fields and magnetization are not synchronized in time. An implicit and stable iterative algorithm was previously developed by the authors [42], combining the efficient grid implementation of the Maxwell and LLG equations and an implicit and iterative solver for the LLG equation [41,49]. A similar FDTD LLG numerical scheme is adopted here, but using a rather faster explicit algorithm, as follows:

(1) Evaluate $\mathbf{B}^{n+1/2}$ from Maxwell's Eqs. (13) and (14) using the previous computed values of electric field $\mathbf{E}^n$ and magnetic flux density $\mathbf{B}^{n-1/2}$. The magnetic flux density at time-step n can then be computed from the time average

$$\mathbf{B}^n = \frac{\mathbf{B}^{n+1/2} + \mathbf{B}^{n-1/2}}{2}.$$

(2) Evaluate $\mathbf{B}^n$ at the grid locations of $\mathbf{M}$ (i.e., cell corners) using two-point spatial interpolations. For example, B_x is determined at the magnetization cell corner using the spatial average along the x direction:

$$B_x|_{i,j}^n = \frac{B_x|_{i+1/2,j}^n + B_x|_{i-1/2,j}^n}{2}.$$

Similar interpolation is performed to determine $B_y|^n_{i,j}$.

(3) Evaluate the effective field $\mathbf{H}_{\text{eff}}$ at time-step $n-1/2$ using the previously computed magnetization:

(i) Update the exchange boundary conditions described in Eq. (10) at the magnetic material interfaces using second-order central differences. For example, on the left-hand boundary of the TMz grid in Fig. 1, the magnetic boundary condition can be approximated by

$$\left.\frac{\partial \mathbf{M}}{\partial x}\right|_{i,j} \approx \frac{\mathbf{M}|_{i+1,j} - \mathbf{M}|_{i-1,j}}{2\Delta x} = 0,$$

to define the magnetization just exterior to the magnetic material boundary (left and right boundaries in this example):

$$\mathbf{M}|_{i+1,j} = \mathbf{M}|_{i-1,j}. \tag{19}$$

These exterior points are needed for the evaluation of the exchange fields next.

(ii) Evaluate the exchange field using the second-order accurate central finite-difference approximation:

$$\mathbf{H}_{\text{ex}}|_{i,j} \approx \frac{2A}{\mu_0 M_s^2 \Delta x^2}\begin{pmatrix}\mathbf{M}|_{i+1,j} + \mathbf{M}|_{i-1,j} + \mathbf{M}|_{i,j+1} \\ +\mathbf{M}|_{i,j-1} - 4\mathbf{M}|_{i,j}\end{pmatrix}, \tag{20}$$

where the last term on the right-hand side is due to the spatially invariant magnetization in the z direction in the two-dimensional TMz mode. The magnetization points located in free space just outside of the boundary are substituted using the exchange boundary condition in Eq. (19).

(iii) Evaluate the anisotropy field $\boldsymbol{H}_k$ defined in Eq. (11) using the magnetization values at the FDTD cell corners.

(iv) Evaluate the internal Maxwell fields using the constitutive relation

$$\mathbf{H}(\mathbf{M}^{n-1/2}) = \mathbf{B}^{n-1/2}/\mu_0 - \mathbf{M}^{n-1/2},$$

and determine the effective field in Eq. (8) at time-step $n-1/2$.

(4) Evaluate the effective field at time-step n using the extrapolation

$$\mathbf{H}_{\text{eff}}(\mathbf{M}^n) = \frac{3}{2}\mathbf{H}_{\text{eff}}(\mathbf{M}^{n-(1/2)}) - \frac{1}{2}\mathbf{H}_{\text{eff}}(\mathbf{M}^{n-3/2}), \tag{21}$$

which is second-order accurate, while conserving the magnitude of the magnetization [50].

(5) Solve Eq. (18) explicitly for $\mathbf{M}^n$ using the previously computed magnetization $\mathbf{M}^{n-1/2}$ and extrapolated effective field $\mathbf{H}_{\text{eff}}(\mathbf{M}^n)$ at the grid corners using [41]

$$\mathbf{M}^n = \frac{\mathbf{M}^{n-1/2} + (\mathbf{a}\cdot\mathbf{M}^{n-1/2})\mathbf{a} - \mathbf{a}\times\mathbf{M}^{n-1/2}}{1+|\mathbf{a}|^2}, \tag{22}$$

where $\mathbf{a} = -\left[\frac{|\gamma|\Delta t}{2}\mathbf{H}_{\text{eff}}(\mathbf{M}^n) + \frac{\alpha}{M_s}\mathbf{M}^{n-1/2}\right]$.

(6) Evaluate $\mathbf{M}^{n+1/2}$ using extrapolation $\mathbf{M}^{n+1/2} = 2\mathbf{M}^n - \mathbf{M}^{n-1/2}$.

(7) Evaluate $\mathbf{M}^{n+1/2}$ at the location of the $\boldsymbol{B}^{n+1/2}$ field using two-point spatial interpolations, as described earlier, and then calculate the corresponding $\boldsymbol{H}^{n+1/2}$ field from

$$\mathbf{H}^{n+1/2} = \mathbf{B}^{n+1/2}/\mu_0 - \mathbf{M}^{n+1/2}.$$

(8) Finally, evaluate electric field $\mathbf{E}^{n+1}$ using Eq. (15).

This algorithm is second-order accurate, and therefore, consistent with the second-order nature of the leapfrog time-marching scheme of the FDTD method. This scheme is also stable and bound by the Courant stability limit of the FDTD method, which imposes the following restriction on the time-marching step size Δt [29]:

$$\Delta t \le \frac{\Delta x}{c\sqrt{\text{dim}}}, \tag{23}$$

where c is the speed of light in vacuum and dim is the dimensionality of the system and is equal to two for the TMz mode considered here. The spatial increment Δx in the FDTD grid is normally chosen to sufficiently sample the shortest wavelength in the simulation space and/or smallest physical and electromagnetic feature in the simulated materials (such as skin depth, exchange length, or domain wall width in a magnetic material). The Courant stability criterion in Eq. (23) is generally very stringent, and hence, provides a sufficiently small time step to ensure stability of integration of the LLG equation, and therefore, of the complete FDTD-LLG algorithm, as demonstrated in the next section.

IV. SIMULATION RESULTS AND DISCUSSION

This work is concerned with studying the magnetization dynamics and resonance from the electromagnetic wave interaction with infinite cobalt nanoprisms with square cross sections of side lengths 50–1000 nm. The magnetic parameters used in the FDTD-LLG simulations for cobalt are $M_s = 1.422\times10^6$ A/m, $A = 3.1\times10^{-11}$ J/m [51], $K_1 = 450\times10^3$ J/m^3, and $K_2 = 150\times10^3$ J/m^3 [52]. The damping coefficient in the LLG equation is set to $\alpha = 0.02$ to speed up the convergence to the minimum-energy state. A constant value of electrical conductivity of 1×10^7 (Ω

m)$^{-1}$ is used for cobalt in the simulations, which is within the range of published values for thin-film and bulk material [53]. The constant electrical conductivity also ensures a consistent nonmagnetic skin depth for the different prism sizes to study the magnetic skin effect from power absorption spectra.

Using the magnetic material parameters for cobalt yields an exchange length $L_{ex} = 5$ nm. Hence, a square-grid cell size of $\Delta x = 5$ nm is used in the FDTD LLG simulations. This is to sufficiently sample the spatial magnetization distributions, domain structure, and skin depths within the structure, while providing practical computational times. A grid cell size of $\Delta x = 2.5$ nm is also tested in a separate simulation for the smallest prism size (50 nm) for validation and yields negligible effects on the distribution and spectra of the computed magnetization and fields. The cell size $\Delta x = L_{ex}$ is also sufficient to provide a smooth magnetization distribution in the corners of the simulated prisms, as diverging exchange and magnetostatic fields are balanced over shorter TMz scales [54]. According to the Courant stability limit in Eq. (23) for the two-dimensional TMz mode considered here, the corresponding time step $\Delta t = \Delta x/2c = 8.3 \times 10^{-18}$ s is used to ensure numerical stability of the time-marching scheme in the FDTD method and accurate computation of the electromagnetic fields [29]. This time step also naturally satisfies the stability requirement for the accurate time integration of the LLG equation and effective sampling of all relevant resonance modes. A simulation time of 1 ns is used to capture the transient magnetization response and achieve convergence of the normalized magnetic energy $|\mathbf{M} \times \mathbf{H}_{eff}|/M_s^2$ to a minimum of 10^{-6} or less and approach equilibrium of the electromagnetic fields (with $\mathbf{E} \to 0$) [41]. The small time step stipulated by the Courant limit and the exchange length in the FDTD simulations lead generally to large computational times (the extent depends on the numerical implementation and hardware resources). This time-step restriction in the FDTD method can be relaxed to reduce computational times by using unconditionally stable time-marching schemes, such as the alternating-direction implicit (ADI) scheme [29,30].

A dc field $\mu_0 H_z = 200$ mT is applied along the prism axis to saturate the structure and operate in the linear magnetic regime. The initial direction of magnetization in the simulations is parallel to the applied dc field along the z axis, as indicated in Fig. 2. The y-directed z-polarized plane electromagnetic wave is applied from the lower TFSF boundary with normal incidence on the prism lower surface, as shown in Fig. 2. The Gaussian pulse profile described in Eq. (17) is used to excite the plane wave with a small amplitude of $\mu_0 H_0 = 0.1$ mT to operate in the linear magnetic regime and to minimize field reflections from the PML boundaries. The Gaussian source has a bandwidth of $f_c = 70$ GHz (at which the square magnitude of its Fourier transform reduces to e^{-1} of its maximum) set by the pulse width $\tau = 1/(\sqrt{2}\pi f_c) = 3.2 \times 10^{-12}$ s. This pulse is also sufficiently sampled by the time step Δt in FDTD-LLG simulations. At this frequency, the nonmagnetic skin depth for cobalt is $1/\sqrt{\pi f \mu_0 \sigma} \sim 600$ nm.

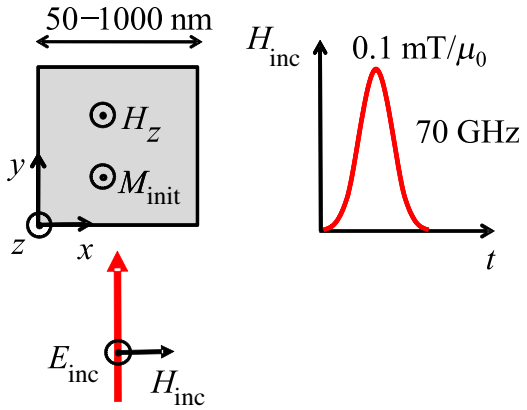

FIG. 2. Semi-infinite cobalt prism and incident plane wave source and time profile.

A. Dynamic magnetization

The transient magnetization for some of the simulated cobalt prisms is illustrated in Fig. 3, shortly following application of the electromagnetic wave pulse. The vector arrow plot shows the x and y components of the dynamic magnetization, and the contour plot represents the magnetic flux density distribution. The z-polarized incident tangential electric field induces an axial current density inside the prism that results in a curling (or circumferential) nonuniform internal magnetic field that increases in magnitude with distance r from the center of the prism, according to $H \sim J_z r/2$, where $J_z = \sigma E_z$ is the current density. Hence, the induced internal curling magnetic field increases with increasing prism size, as observed in Fig. 3, with the exception of prisms larger than the nonmagnetic skin depth ($\sim$600 nm), where the incident electromagnetic fields are attenuated. The internal curling magnetic field produces a curling magnetization distribution that continuously changes chirality through intermediate and reversing diverging distributions during precession, as illustrated in Fig. 3. The small transverse magnetic field component of the incident plane wave has a negligible effect on dynamic magnetization, which is mainly coupled to the axial electric field (corresponding to the case of longitudinal magnetoimpedance in conductive magnetic wires) [26].

The magnetization curling mode (CM) in Fig. 3 is confirmed to result from the axially generated current density in the conductive prisms, since it is not observed when the conductivity of the material is set to zero in separate simulations. Figure 4 illustrates simulation

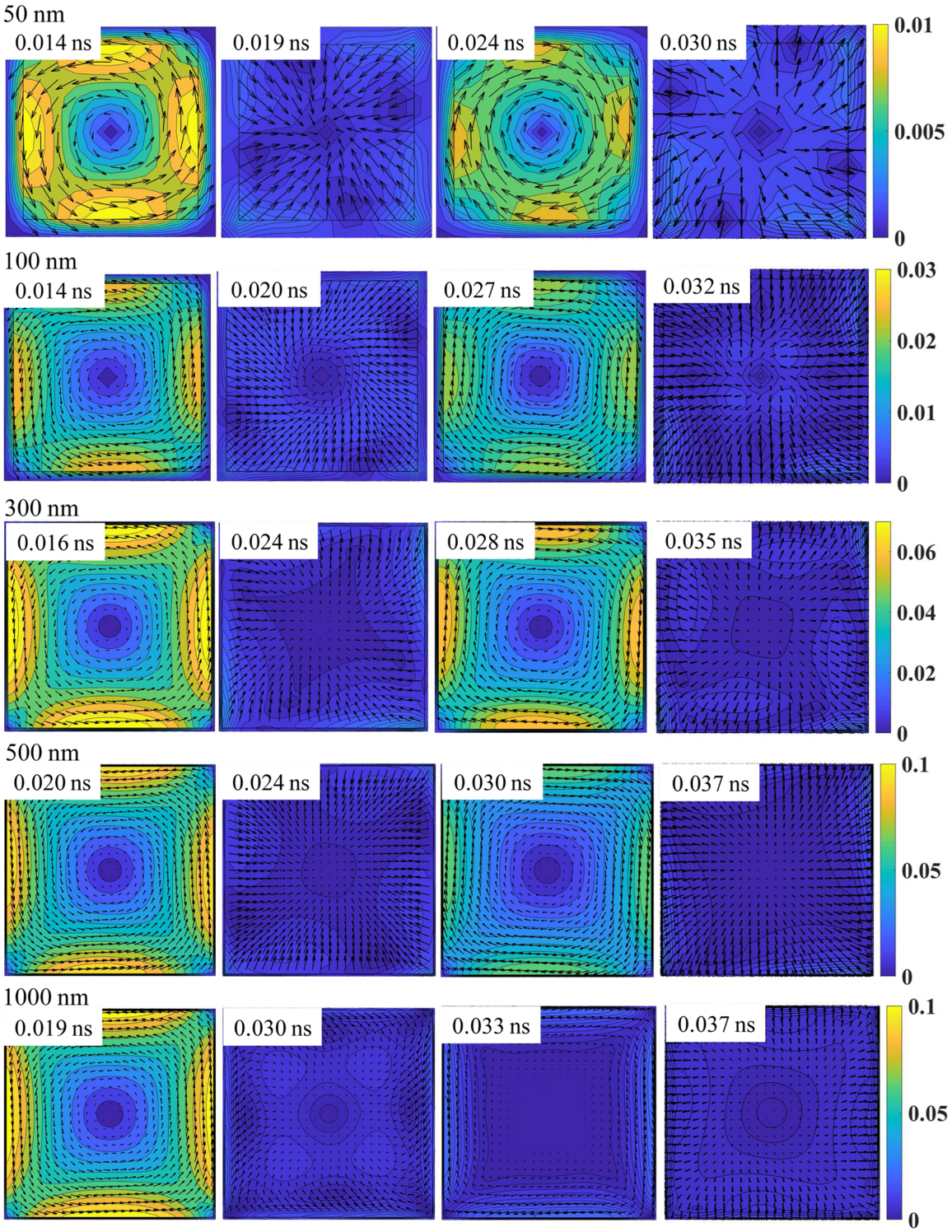

FIG. 3. Vector arrow plot of dynamic magnetization (x and y components) in cobalt prisms with different side lengths shortly following excitation by a 70 GHz Gaussian electromagnetic plane wave. Contour plot is the instantaneous magnitude of calculated magnetic flux density (in tesla).

results for a 300 nm cobalt prism with zero conductivity, showing uniform magnetization precession excited by the transverse magnetic field component of the incident plane wave. The magnetization curling mode is also more energetically favorable here, since the smallest prism size used in this work (50 nm) is larger than the critical radius for nucleation of the curling mode in long cylindrical structures [16]. The critical radius for

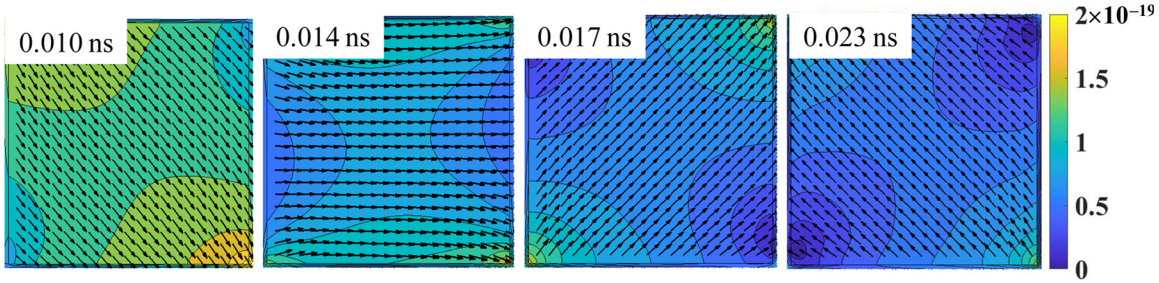

FIG. 4. Simulated dynamic magnetization for a 300 nm insulated prism during and following excitation by a 70 GHz Gaussian electromagnetic plane wave, illustrating the uniform magnetization precession in the absence of electrical conductivity, where oscillations are mainly coupled with the transverse magnetic field of the applied plane wave. Contour plot is the calculated magnetic flux density (in tesla).

the curling mode can be estimated from matching the nucleation fields of the uniform (dipolar) and nonuniform (exchange) modes and is equal to (for the first eigenvalue in the solution) $R_c = 1.8412\sqrt{2A/\mu_0 M_s N}$ [16], where $N = 1/2$ is the demagnetizing factor for the infinite cylinder. Using the parameters for cobalt yields a critical radius of $R_c \sim 13$ nm, which is less than the smallest prism size of 50 nm considered here. Following application and decay of the incident Gaussian pulse, the current-induced internal fields will be altered by the demagnetizing, exchange, and eddy current fields, leading to nonuniform magnetic and electric field distributions and complex magnetic configurations and resonance modes. The magnetization and magnetic field configurations for the different prism sizes are studied next to examine the resonance mechanisms and their size dependence.

1. Prism side lengths ≤100 nm

When the prism side lengths are less than the nonmagnetic skin depth, the incident tangential electromagnetic fields are expected to penetrate through the full prism volume. For prism side lengths ≤100 nm, the diverging magnetization distributions during precession reduce the exchange energy, but yield surface charges that increase the demagnetizing fields, particularly in the prism edges. It can be further observed in Fig. 3 that the flux closure in the CM is incomplete due to the noncircular induced current distribution through the prism cross section, leading to localized surface charges near the corner regions that increase the local power absorption (see Sec. IV B). The curling magnetization mode also increases the exchange energy to align neighboring spins. The dipolar and exchange contributions both lead to azimuthal and radial spin waves [17]. The resonance frequencies of the CM over this size range may be modeled following the exchange curling derivation of Brown [16] for the saturated infinite circular cylinder with radial demagnetizing fields. In this case, the linearized Landau-Lifshitz equations (without damping), including $e^{j\omega t}$ time dependence, can be written in cylindrical coordinates as

$$\frac{j\omega}{\gamma} m_r + (H_z + M_s g + M_s L_{\rm ex}^2 k_s^2) m_\theta = 0, \quad (24a)$$

$$(H_z + M_s + M_s g + M_s L_{\rm ex}^2 k_s^2) m_r - \frac{j\omega}{\gamma} m_\theta = 0, \quad (24b)$$

where m_r and m_θ are the radial and azimuthal magnetization perturbations in the circular cylinder, respectively; $g = 2K_1/\mu_0 M_s^2$ is the uniaxial magnetocrystalline anisotropy factor (second anisotropy term is negligibly small near saturation); $L_{\rm ex} = \sqrt{2A/\mu_0 M_s^2}$ is the exchange length; and k_s are the spin-resonant wave numbers. The M_s term in the coefficient of m_r in Eq. (24b) represents the radial demagnetizing field [26]. The nontrivial solution of Eq. (24) requires that the determinant of the coefficients of the magnetization be zero, yielding the CM resonance frequency:

$$\omega_{\rm CM} = \gamma \sqrt{(H_z + M_s g + M_s L_{\rm ex}^2 k_s^2)(H_z + M_s + M_s g + M_s L_{\rm ex}^2 k_s^2)}. \quad (25)$$

Assuming solutions of magnetization in the form $e^{j\theta} J_1(k_s r)$ with azimuthal symmetry, where J_1 is the Bessel function of the first kind, and applying the unpinned (exchange) boundary condition $d\mathbf{m}(r,\theta)/dr = 0$ at the cylinder radius $r = R$, yields the spin-resonant radial wave numbers k_s from the solutions of $J_1'(k_s R) = 0$. The CM resonance frequencies in Eq. (25) include a dependence on the prism size through the exchange term. Kraus [23] has shown that the secular equation for electromagnetic wave excitation in the circular cylinder is the same as that for planar wave excitation. This explains the similarity of Eq. (25) to Kittel's ferromagnetic resonance frequency for planar structures without exchange [14] and was therefore suggested by Kraus [23] to describe the resonance frequency for the rotationally symmetric (curling) resonance mode in long cylinders.

To make a valid comparison between the resonance frequencies for the circular cylinder in Eq. (25) to the square

prism considered here, the equivalent cylinder radius that yields the same demagnetizing factor (or demagnetizing energy) for the square prism needs to be estimated [55]. For a circular cylinder with axial length L and radius R, a series expansion of its axial demagnetizing factor for large L to first-order yields $N_z^{\rm cyl} \approx \zeta_{\rm cyl} R/L$, where $\zeta_{\rm cyl} = 8/3\pi$ [55]. The demagnetizing factors for a saturated square prism with axial length L and side length W can be generally found analytically in Refs. [55,56]. Expanding the axial demagnetizing factor for infinite prism length L to first-order yields $N_z^{\rm pri} \approx \zeta_{\rm pri} W/L$, where $\zeta_{\rm pri} = [1 - \sqrt{2} + 3\sinh^{-1}(1)]/2$. The remaining components of the demagnetizing factors for the long circular cylinder and square prism can then be easily obtained using $N_x = N_y = (1 - N_z)/2$. Equating the first-order series expansions of the axial demagnetizing factors for the cylinder and prism provides analytically the equivalent cylinder radius of a square prism as $2R \approx 1.11\ W$. Considering the 50 and 100 nm cobalt prisms with applied field $\mu_0 H_z = 200$ mT, and using the first (fundamental) wave number $k_s R = 1.8412$ and equivalent cylinder radii in Eq. (25), yields the CM ferromagnetic resonance frequencies $\omega_{\rm CM}/2\pi \approx 48$ and 43 GHz, respectively. Figure 5 plots the local computed spectra of the transient M_x from the FDTD-LLG simulations, which are evaluated at the center of the prism edges (10 nm from the lower prism boundary), showing the resonance peaks for the different prism sizes. Figure 5 demonstrates excellent agreement between the simulated fundamental resonance peak frequencies for prism sizes of $\leq$100 nm and the theoretical CM frequencies calculated using Eq. (25) (vertical dashed lines). It will be shown in Sec. IV B that Eq. (25) is also able to accurately predict the higher-frequency spin-wave modes, in agreement with the FDTD-LLG simulations. The discussion of spin-wave modes is postponed to Sec. IV B, as it better reflects the dominant spin-wave modes integrated over the prism cross sections, rather than the localized magnetization spectra.

2. Prism side lengths >100 nm

With increasing prism side lengths beyond 100 nm, it can be observed in Fig. 3 that the magnetic response becomes more confined to the prism edges and the x-y magnetization is reduced towards the center of the prism. This happens even for prism sizes smaller than the nonmagnetic skin depth. This can be attributed to magnetization precession in the prism edges excited by the current-induced circumferential fields, leading to an increase in the local imaginary permeability and wave vectors that attenuate propagating waves to depths that are fractions of the nonmagnetic skin depth at resonance [20,24]. This magnetic skin depth is estimated in Sec. IV B from the simulated local power absorption spectra.

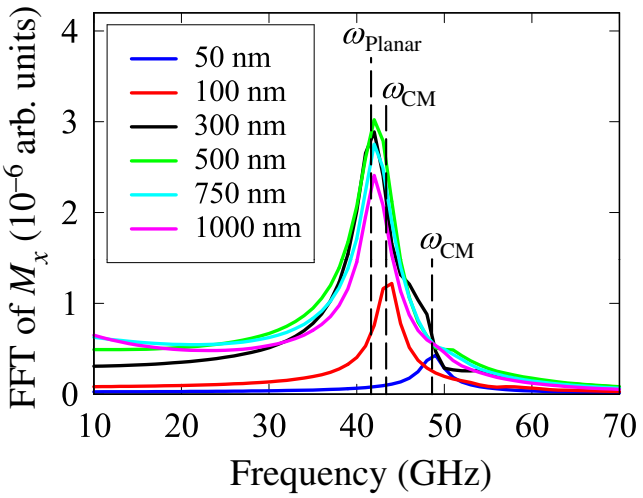

FIG. 5. Fourier transforms of computed M_x at the center of the lower edge of the square cobalt prisms from FDTD-LLG simulations. Dashed vertical lines indicate the theoretical ferromagnetic resonance frequencies for magnetization curling ($\omega_{\rm CM}$) in the infinite equivalent cylinder and in a thin planar film ($\omega_{\rm planar}$) predicted using Eqs. (25) and (26), respectively.

To study the magnetic response in the confined edge regions, Fig. 6 illustrates the simulated transient magnetization and internal fields along the lower edge of the 300 nm prism (10 nm from the lower prism boundary). In Fig. 6, M_x is the tangential magnetization component in the edge stripe and M_y is the normal component. The magnetization and fields at $t = 0.01$ ns correspond to the peak of the incident Gaussian pulse, producing a maximum internal circumferential magnetic field with tangential component (blue line) $H_x \sim J_z r/2 \sim 0.015 M_s$, corresponding to the field from a current-carrying wire. This plot again confirms that the edge-mode resonance is excited by the induced axial current. The remaining plots in Fig. 6 are taken during different cycles following decay of the Gaussian source. Focusing on the M_x component in Fig. 6, the transient magnetization is mostly uniform in the central region of the edge, with increased and uneven pinning in the corner regions. Figure 6 also indicates low-intensity odd standing spin-wave modes in the confined edge regions [57,58]. The observed reduction in x-y magnetization in the corners, and hence, pinning, can be explained by the parallel alignment of magnetization along the prism axis (z direction) in the corners to minimize surface charges, in the absence of demagnetizing fields in the axial direction. The increased pinning in the lateral boundaries is also consistent with the reduction of the thickness to width aspect ratio of the circumferential regions with increased prism size, which increases the pinning coefficient in the generalized Rado-Weertman magnetic boundary description [19] due to dipolar and surface anisotropy effects [59]. Pinning in the corners here, which can be treated as a z-directed

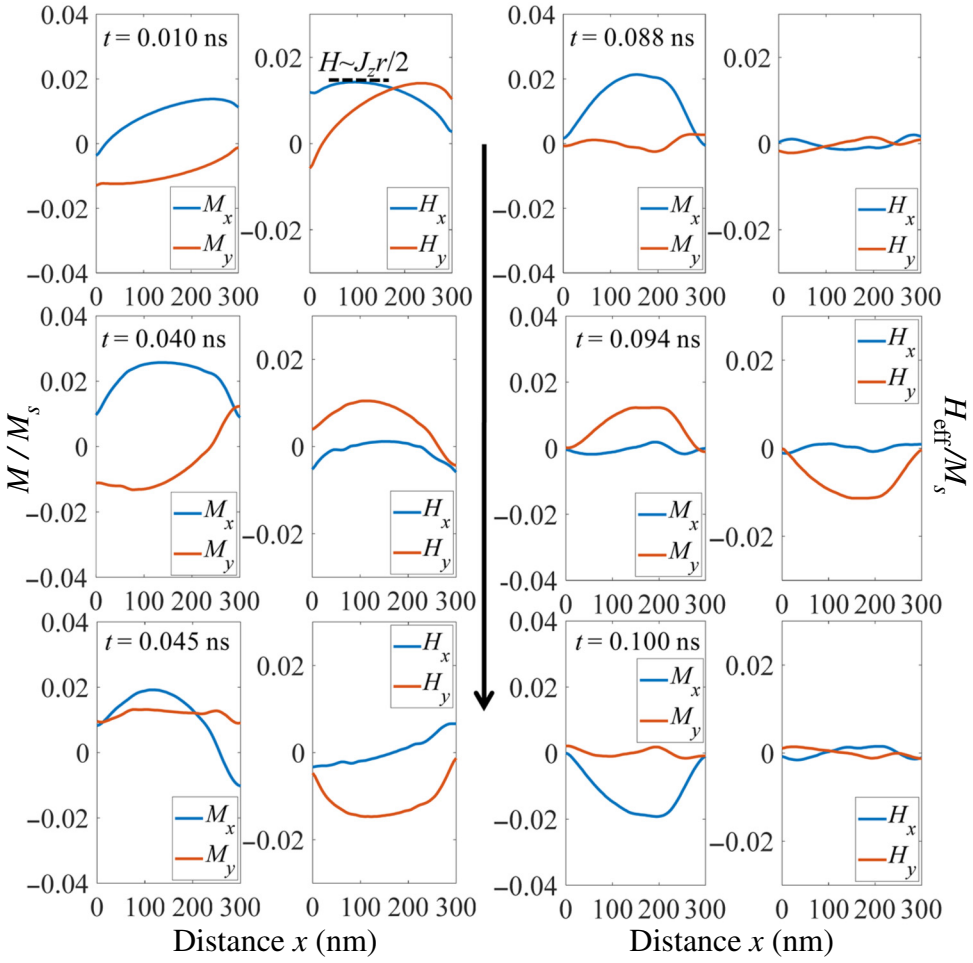

FIG. 6. Transient magnetization and effective fields along the lower edge of the 300 nm prism (at a distance of 10 nm away from its lower boundary and within the confined magnetic region), following excitation and decay of the applied Gaussian wave. First plot at $t = 0.01$ ns is taken at the peak of the applied Gaussian pulse, showing that internal fields are produced by the induced axial current.

surface anisotropy in the lateral parts of the edge region, increases with time, as observed in Fig. 6 due to the decay of the Gaussian wave source and reduction of the internal circumferential fields. Figure 7 illustrates the vector magnetization in the 300 nm prism over half a precession cycle, showing clearly the reduction in x-y magnetization in the corners and center of the prism. Figure 7 also shows reversal in the axial current direction due to the reciprocal effect of chirality reversal of the circumferential magnetization and resulting magnetic fields. The

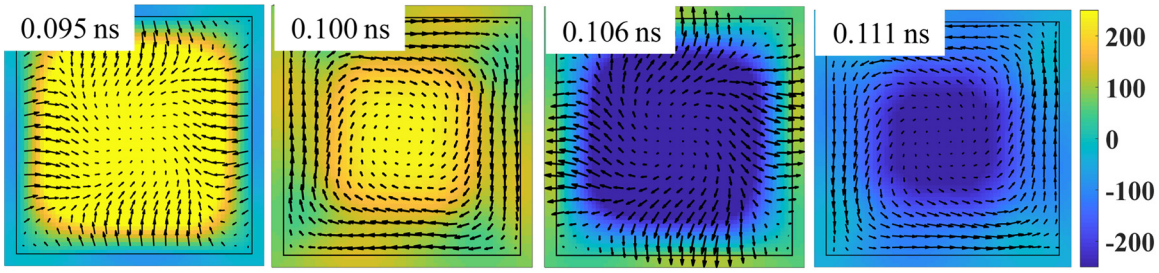

FIG. 7. Vector arrow plot of transient magnetization in the 300 nm prism following decay of the applied Gaussian wave, showing confinement of magnetization around the prism circumference within a magnetic skin depth. There is also reduction of x-y magnetization in the corner regions (pinning) and in the central region of the prism. Intensity plot represents the transient electric field (in V/m), which reverses direction following reversal in the circumferential magnetization.

frequency of this reversal in electric field, hence, matches the fundamental precession frequency of magnetization in the central region of the prism edges, which is about 42 GHz for prism sizes of ≥300 nm, as indicated in Fig. 5.

The confined magnetic regions along the prism circumference can be approximated by rectangular stripe geometries with width W and thickness d, where $W > d$. The current-induced circumferential fields excite predominantly uniform magnetization precession in the stripes (see Figs. 6 and 7) and lower-intensity standing spin-wave modes with quantized wave numbers determined by the boundary conditions [60,61]. To study and analyze the resonance mechanisms and frequencies in the confined edge regions of the prism, the thin stripe regions can be divided into a central elongated part and a localized corner part. In the central region, the magnetization precession is mostly uniform and increases in intensity with increasing prism size. The resonance frequency here can be written for a saturated planar structure in the form [14]

$$\omega_{\text{Planar}} \approx \gamma\sqrt{(H_z + M_s g + M_s N_x)(H_z + M_s g + M_s N_y)}, \tag{26}$$

where N_x and N_y are the demagnetizing factors along the width and thickness of the central region of the stripe, respectively. Using the local demagnetizing factors for a rectangular prism derived by Joseph and Schlömann [62] and Smith *et al.* [63], and expanding to first order for infinite axial length, yields the demagnetizing factors in the center of the thin stripe as $N_x \sim 0$ and $N_y \sim 1$ (thin-film structure). For cobalt prisms, this yields $\omega_{\text{planar}}/2\pi \approx 42$ GHz which is in excellent agreement with the peak frequencies of the simulated magnetization spectra in Fig. 5 for prism sizes of ≥300 nm. The quantized exchange spin-wave wave numbers in the confined edge regions along the prism side length W (assuming uniform magnetization through thickness d of the stripe) can be generally written for p half-wavelength nodes as $k_x = p\pi/W$. With increasing prism side lengths of $W \geq 300$ nm, the quantized wave numbers, and hence, exchange spin-wave contribution (or intensity), become negligibly small for any lateral boundary condition, as observed from the FDTD-LLG spectra in Fig. 5 and magnetization profiles in Fig. 6. The decrease in wave numbers reduces the frequency shift between the quantized spin-wave modes with frequencies degenerating to the fundamental mode in Eq. (26) with further increases in prism size. This leads to the observed widening of the fundamental resonance peak in the magnetization spectrum in Fig. 5 for the 300 nm prism towards higher frequencies. For prisms sizes of >300 nm, the higher-frequency exchange modes are also not visible in the simulated power absorption spectra (discussed in Sec. IV B in Fig. 10). Hence, the exchange spin-wave contribution will be assumed to be negligibly small in the circumferential stripe regions for the prism sizes used here.

Turning to the corners in the confined edge regions of the cobalt prisms, Fig. 8(a) illustrates the spectrum of magnetization in the corner of the 300 nm prism and shows the appearance of a higher-frequency resonance peak at about 48 GHz (in addition to the thin-film resonance peak at 42 GHz). The corner resonance peak is not observed in the spectrum of the magnetization in the central region of the prism edge [shown for comparison in Fig. 8(a)]. The frequency and intensity of this corner mode are also found to be size independent for all prism sizes of >100 nm. To further confirm this corner mode, separate FDTD-LLG simulations of sinusoidal electromagnetic wave excitation

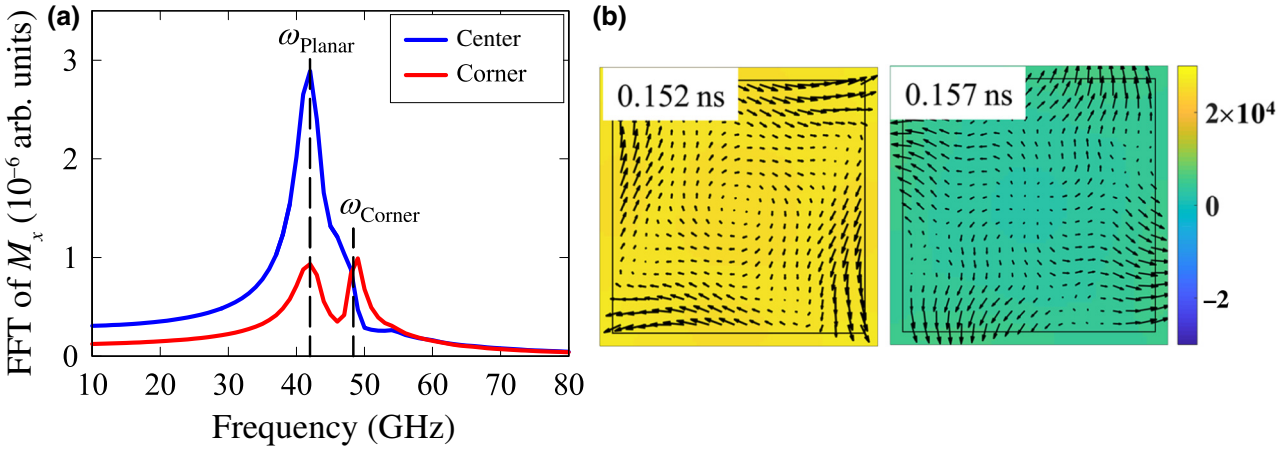

FIG. 8. (a) Calculated spectrum of M_x for the 300 nm cobalt prism, evaluated in the center (blue line) and corner (red line) regions of the prism edge, showing a high-frequency peak at 48 GHz due to corner-mode precession. (b) Simulated vector plot of magnetization in the 300 nm cobalt prism excited using a sinusoidal electromagnetic plane wave at the corner frequency of 48 GHz, confirming excitation of uniform corner-mode precession. Color plot represents the electric field distribution due to the applied sinusoidal electromagnetic wave (in V/m).

at 48 GHz are carried out for the 300 nm cobalt prism (using the same field amplitude of the Gaussian pulse). The resulting transient magnetization distribution in Fig. 8(b) confirms the excitation of uniform magnetization precession localized in the corner regions of the prism. The theoretical resonance frequency in the corners can be estimated from Eq. (26) using the local demagnetizing factors for a rectangular prism [62,63], expanded to first order for infinite axial length, and evaluated near the corners (over a region of few exchange lengths) to yield $N_x = N_y \sim 1/2$. Substituting the demagnetizing factors in Eq. (26) gives the approximate corner resonance frequency:

$$\omega_{\text{corner}} \approx \gamma(H_z + M_s g + M_s/2). \tag{27}$$

Using the parameters for cobalt in Eq. (27) yields $\omega_{\text{corner}}/2\pi \approx 48$ GHz, shown as the dashed vertical line in Fig. 8(a), and is in excellent agreement with the simulated resonance peak in the corner region. This agreement confirms the uniform resonance mode in the corners of the confined circumferential regions of the prism.

As prism sizes increase beyond the nonmagnetic skin depth (∼600 nm), there is attenuation of the propagating electromagnetic waves, and therefore, a reduction in the current-induced circumferential fields in the prism. Figure 9 plots the simulated transient electric fields at the center of the cobalt prisms and illustrates the attenuation of the incident fields for prisms larger than the nonmagnetic skin depth. Figure 9 also illustrates the attenuation of the propagating fields for prisms with side lengths of $100\text{ nm} < W < 600\text{ nm}$ due to the magnetic skin effect described earlier. The large oscillations in the electric fields for prisms ≥300 nm are due to the reciprocal effect of chirality reversal of magnetization in the prism edges, with

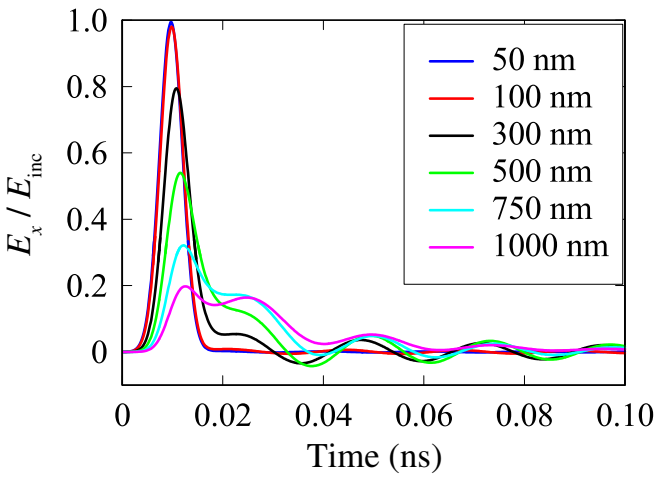

FIG. 9. Simulated normalized electric field at the center of the cobalt prism for different prism sizes, showing attenuation of fields due to skin-depth effects (nonmagnetic and magnetic) and electric field oscillations due to reversal of the circumferential magnetization.

a frequency that equals the precession frequency of magnetization in the central region of the prism edges predicted by Eq. (26) (∼42 GHz). The attenuation of electric fields in prism sizes greater than the nonmagnetic skin depth causes a reduction of the induced circumferential magnetic field, and hence, in the intensity of the local magnetization spectra, as observed in Fig. 5 for 750 and 1000 nm prisms. Figure 5 further shows an increase of the dc content in the local magnetization spectra with increasing prism sizes, which is due to the increase of the spectral magnitude of the current-induced Gaussian internal magnetic fields with increasing prism size.

B. Power absorption spectra

The aim of this section is to calculate and study the local distribution and integrated spectra of the absorbed electromagnetic energy by magnetization in the cobalt prisms from transient FDTD-LLG simulations. Starting with Poynting's theorem, the equation for electromagnetic energy conservation integrated over volume V of the magnetic material under consideration is given by [64]

$$\int_V \left(\mathbf{H}\cdot\frac{\partial \mathbf{B}}{\partial t} + \mathbf{E}\cdot\frac{\partial \mathbf{D}}{\partial t} + \mathbf{E}\cdot\mathbf{J}\right) dV = -\int_V \nabla\cdot(\mathbf{E}\times\mathbf{H}) dV. \tag{28}$$

Substituting $\mathbf{B} = \mu_0(\mathbf{M}+\mathbf{H})$ and $\mathbf{D} = \varepsilon_0\mathbf{E}$ into Eq. (28) (assuming for simplicity real and frequency-independent permittivity) yields

$$\int_V \left[\frac{\partial}{\partial t}\left(\mu_0\mathbf{H}\cdot\frac{\partial \mathbf{H}}{\partial t} + \varepsilon_0\mathbf{E}\cdot\frac{\partial \mathbf{E}}{\partial t}\right) + \mathbf{E}\cdot\mathbf{J} + \mu_0\mathbf{H}\cdot\frac{\partial \mathbf{M}}{\partial t}\right] dV = \int_V -\nabla\cdot(\mathbf{E}\times\mathbf{H}) dV. \tag{29}$$

The first term on the left-hand side of Eq. (29) represents the rate of change of stored energy in the magnetic and electric fields in the medium per unit volume per unit time. The second term represents the classical resistive loss in the conductive magnetic structure. The third term is the energy absorbed by magnetization $\mathbf{M}$ placed in magnetic field $\mathbf{H}$ per unit volume per unit time, which is of interest here [65]. The left-hand side of energy conservation in Eq. (29) is balanced by energy flowing into volume V represented on the right-hand side by the divergence of the Poynting vector $\mathbf{E}\times\mathbf{H}$.

To evaluate the spectra of the energy absorbed, complex harmonic fields with a time dependence of $e^{j\omega t}$ are now considered and energy conservation in Eq. (29) becomes [64]

$$\frac{1}{2}\int_V [j\omega(\varepsilon_0 E^2 - \mu_0 H^2) + \mathbf{E}\cdot\mathbf{J}^* - j\omega\mu_0\mathbf{M}\cdot\mathbf{H}^*] dV = \frac{1}{2}\int_V -\nabla\cdot(\mathbf{E}\times\mathbf{H}^*) dV, \tag{30}$$

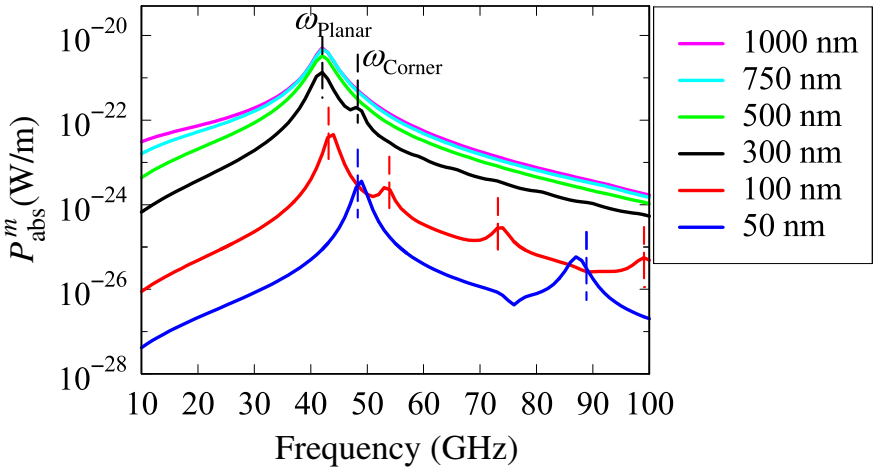

FIG. 10. Simulated total absorbed power per unit length in the cobalt prisms. Vertical dashed lines represent theoretical resonance frequencies calculated using Eq. (25) for the curling mode (ω_{CM}, for the 50 and 100 nm prisms), and using Eqs. (26) and (27) for resonance modes in the center (ω_{planar}) and corners (ω_{corner}) of the thin confined regions along the prism edges, respectively (for prisms of $\geq$300 nm).

where * indicates the complex conjugate of the harmonic field. The real part of the field products in Eq. (30) is normally taken to evaluate the time-averaged power densities. Hence, the real part of the Poynting vector on the right-hand side of Eq. (30) gives the resistive (ohmic) loss, while the imaginary part represents the energy stored and absorbed by the fields and magnetization, respectively. The time-averaged power absorbed by magnetization in the prisms is therefore $1/2\text{Re}(j\omega\mu_0\mathbf{M}\cdot\mathbf{H}^*)$, and the total power absorbed over the prism volume is given by

$$P^m_{\text{abs}} = \frac{1}{2}\text{Re}\int_V j\omega\mu_0\mathbf{M}\cdot\mathbf{H}^* dV.$$

The spectrum of the time-averaged total power absorbed by the magnetization is determined from the FDTD-LLG simulations by evaluating the Fourier transforms of the transient magnetization and magnetic fields (interpolated at the location of magnetization in the Yee cell corners of the FDTD grid) and calculating the real part of the power density term, as indicated above at all grid points within the cobalt prism (see Fig. 11). The local power density is then integrated in two dimensions (TMz mode) over the cross section of the prisms to yield the total power absorbed per unit length, as plotted in Fig. 10. Figure 10 clearly shows the shift in fundamental absorption peak frequencies from about 48 GHz for the 50 nm prism to about 42 GHz for prism sizes of $\geq$300 nm, in agreement with the local magnetization spectra in Fig. 5. This size-dependent frequency shift is accompanied by an increase in the absorbed power with increasing prism dimensions up to the nonmagnetic skin depth ($\sim$600 nm), where attenuation of the incident electromagnetic wave reduces further increase in power absorption.

The local power absorption spectra for the different prism sizes at the fundamental (peak) resonance frequencies are illustrated in Fig. 11. The magnetization CM was identified in the previous section as the main resonance mechanism in prisms with side lengths of $\leq$100 nm. Over this size range, power is absorbed in the diagonals of the prism due to exchange where neighboring spins are mostly offset. Furthermore, there is incomplete flux closure due to the noncircular distribution of induced currents and fields inside the prisms. This leads to the local surface charges in the corner regions where power is mostly absorbed at resonance as indicated in Fig. 11 for the 50 and 100 nm cobalt prisms. The first three resonance eigenvalues for the CM were theoretically determined from the unpinned boundary solution for the circular cylinder, $J_1'(k_s R) = 0$,

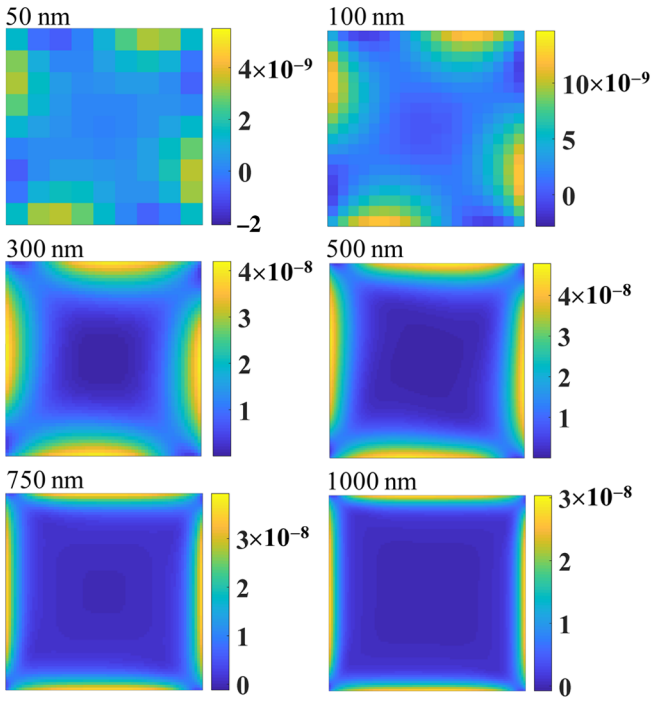

FIG. 11. Calculated local absorbed power density within the cobalt prisms at frequencies of the peak total power absorption indicated in Fig. 10 (48 GHz for 50 nm, 43 GHz for 100 nm, and 42 GHz for the remaining prism cross sections). Color intensity is in units of W/m^3.

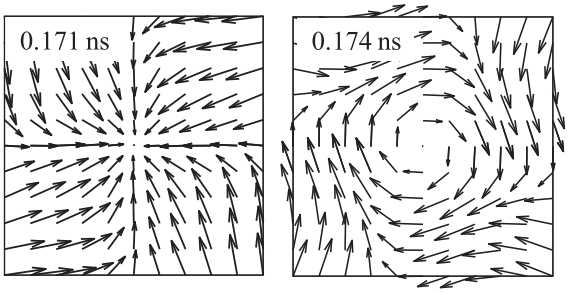

FIG. 12. Plot of vector magnetization in the 50 nm prism from FDTD-LLG simulations following excitation with a sinusoidal electromagnetic wave at a frequency of 76 GHz, corresponding to the minimum observed in the total absorption power spectrum in Fig. 10. Plot shows magnetic configurations that minimize both exchange and magnetostatic energy.

and are given by $k_s R = 1.8412$, 5.3314 and 8.5363, where R is the equivalent radius of the square prism as described in the previous section. The corresponding theoretical resonance frequencies for the 50 nm cobalt prism, determined using (25), are 48, 89, and 161 GHz respectively. These are shown as the dashed vertical lines in Fig. 10 for the 50 nm spectrum and demonstrate very good agreement with the simulated absorption peak frequencies from the FDTD-LLG simulations, particularly at the fundamental mode. There is small discrepancy between theory and simulation at the second eigenfrequency of 89 GHz, which may be attributed to the equivalent cylinder approximation of the prism and disregarding the azimuthal spin-wave modes in the theory. The resonance frequencies in the 100 nm cobalt prism, evaluated using Eq. (25), for the first three eigenvalues are 43, 54, and 73 GHz respectively. These theoretical frequencies are marked as vertical dashed lines in Fig. 10, and are in excellent agreement with the simulated power absorption peak frequencies (even at the fourth eigenfrequency of 99 GHz). Close agreement between the simulated power absorption peak frequencies and CM theory in Eq. (25) confirm that the CM is the main resonance mechanism in cobalt prisms with side lengths of $\leq$100 nm excited by a z-polarized electromagnetic plane wave.

The total power absorption spectrum for the 50 nm prism in Fig. 10 indicates a minimum at 76 GHz. Inspection of the harmonic response at this frequency using a sinusoidal electromagnetic wave excitation (using the same field amplitude as the Gaussian pulse) reveals a number of magnetic configurations that minimize the total magnetic energy. Figure 12 is a vector plot of some of the magnetic configurations during sinusoidal excitation, including the leaf and curling magnetization configurations that attempt to minimize both exchange and magnetostatic energies, and hence, explain the minimum in the power absorption spectrum for the 50 nm prism in Fig. 10.

The local power absorbed in prisms larger than 100 nm is confined to thin regions around the circumference due to skin effects, as observed in Fig. 11. Over this size range, the power absorption is minimum in the center and corner regions of the prism, where magnetization is aligned in the saturated direction along the prism axis. Ferromagnetic resonance is excited in these thin stripe regions by the induced axial current and corresponding circumferential fields. In the center of the thin edge regions, the resonance mechanism is mainly uniform precession, as indicated in Sec. IV A with resonance frequency ω_{planar} given by Eq. (26) for a thin film and is equal to 42 GHz for cobalt. This fundamental frequency is shown in Fig. 10 (dashed vertical line) and is in excellent agreement with the simulated absorption peak frequencies for prism sizes of $\geq$300 nm. The minor power absorption peak at 48 GHz in the 300 nm prism spectrum in Fig. 10 is due to the corner resonance mode, with frequency ω_{corner} predicted accurately using Eq. (27) (shown as a vertical dashed line). The extent of the thin edge regions increases with increasing prism size, leading to the increase of the integrated power absorbed at 42 GHz in Fig. 10. The size of the corner regions remains relatively unchanged with increasing prism size. Hence, the corner-mode minor absorption peak at 48 GHz becomes negligibly small and no longer visible, in comparison to the increasing edge contribution in the spectra of prism sizes of $>$300 nm, as indicated in Fig. 10.

The extent of the confined edge regions observed in Fig. 11 at resonance can be estimated from the spatial profile of local power absorption spectra for prism sizes of $\geq$300 nm. Figure 13 plots these spatial profiles through the center of the cobalt prisms and illustrates the decrease of power absorption towards the center of the prisms. It can be observed in Fig. 13 that power absorption increases with increasing prism size up to the nonmagnetic skin depth. This is due to the increase in current-induced circumferential magnetic field with increasing prism size. Conversely, the power absorption decreases for prisms larger than the nonmagnetic skin depth due to attenuation of the incident electromagnetic fields. The power absorption profiles in Fig. 13 are not exponential, with an approximate linear decrease near the prism surfaces, followed by higher order and sharper decreases than that of the exponential function towards the center of the prisms. However, for consistency with the definition of the nonmagnetic skin depth, the magnetic skin depths at which the absorption profiles in Fig. 13 reduce to e^{-1} of their maximum values at the prism boundary are extracted. The estimated magnetic skin depth is around 50 nm for cobalt prisms at the ferromagnetic resonance frequency of the edge mode ($\sim$42 GHz). This indicates that the magnetic response of the magnetic structure is confined to a thin region determined by the magnetic skin depth at resonance. Knowledge of the skin depth range provides valuable guidance for the design and engineering of lightweight and compact structures and practicable devices operating at ferromagnetic resonance.

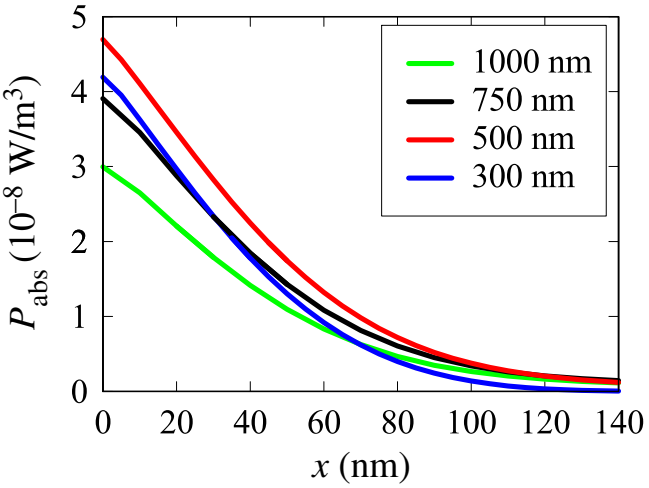

FIG. 13. Simulated local power absorption profiles within cobalt prisms at a fundamental (planar) resonance frequency of 42 GHz. Magnetic skin depth is estimated at e^{-1} reduction in the absorbed power from its peak value and found to be about 50 nm for prism sizes of >100 nm.

V. CONCLUSIONS

Transient electromagnetic-micromagnetic simulations are carried out to study the wide-band electromagnetic wave interaction with infinitely long and conductive cobalt nanoprisms, with square cross sections and side lengths of 50–1000 nm. The focus is on studying the resonance mechanism in the cobalt prisms and their size dependence using the local transient distribution of magnetization and their power absorption spectra. The coupled system of Maxwell's equations and the micromagnetic Landau-Lifshitz-Gilbert equation is solved numerically using a stable algorithm based on the FDTD method. The cobalt prisms are excited with a 70 GHz plane wave at normal incidence and polarization along the prism long axis. The simulations confirm that the dynamic magnetization and resonances are mainly excited by current-induced magnetic fields within the prisms. The magnetization curling mode is identified as the main resonance mechanism in prism sizes of ≤ 100 nm. The size-dependent resonance frequencies and spin-wave modes over this size range are theoretically modeled using an equivalent long circular cylinder with radial demagnetization. For prism sizes beyond 100 nm (but less than the nonmagnetic skin depth), the simulations indicate confinement of the magnetic response to the prism edges due to the magnetic skin effect. This is confirmed by calculations of the local power absorption spectra from the FDTD-LLG simulations, which indicate a magnetic skin depth of approximately 50 nm at the ferromagnetic resonance frequencies of the prisms. The dominant resonance mechanism in the center of the confined edge regions of the cobalt prism is found to be uniform precession with a frequency of 42 GHz, which corresponds to Kittel's ferromagnetic resonance frequency for thin planar structures. The simulations also indicate increased pinning in the corner regions of the prism due to the alignment of magnetization parallel to the prism long axis to reduce the demagnetizing fields. This generates a uniform corner mode with a size-independent resonance frequency of 48 GHz, as indicated by the simulations. This study provides a deeper understanding of the resonance mechanisms in long cobalt nanoprisms and their size dependence. The outcomes of this work provide a valuable insight into the design and engineering of lightweight, compact, and practicable metallic magnetic structures and devices operating at resonance. Moreover, the developed simulation approach (FDTD-LLG) and understanding gained here provides a firm foundation for further studies of electromagnetic wave interaction with three-dimensional and more complex confined metallic magnetic nanostructures, including nonsaturated ground states; different incident wave polarizations, amplitudes, and angles; and arrays and mixtures of dielectric and ferromagnetic constituents.

ACKNOWLEDGMENTS

The authors acknowledge financial support from DSTL and the Engineering and Physical Sciences Research Council (EPSRC) of the United Kingdom, via the EPSRC Centre for Doctoral Training in Electromagnetic Metamaterials (Grant No. EP/L015331/1).

[1] B. Kuanr, R. E. Camley, and Z. Celinski, Effect of shape anisotropy on stop-band response of Fe and permalloy based tunable microstrip filters, IEEE Trans. Magn. **40**, 2841 (2004).

[2] A. Encinas, M. Demand, L. Vila, L. Piraux, and I. Huynen, Tunable remanent state resonance frequency in arrays of magnetic nanowires, Appl. Phys. Lett. **81**, 2032 (2002).

[3] A. Saib, D. Vanhoenacker-Janvier, I. Huynen, A. Encinas, L. Piraux, E. Ferain, and R. Legras, Magnetic photonic band-gap material at microwave frequencies based on ferromagnetic nanowires, Appl. Phys. Lett. **83**, 2378 (2003).

[4] V. Boucher and D. Ménard, Effective magnetic properties of arrays of interacting ferromagnetic wires exhibiting gyromagnetic anisotropy and retardation effects, Phys. Rev. B **81**, 174404 (2010).

[5] Y. Shirakata, N. Hidaka, M. Ishitsuka, A. Teramoto, and T. Ohmi, High permeability and low loss Ni–Fe composite material for high-frequency applications, IEEE Trans. Magn. **44**, 2100 (2008).

[6] Y.-B. Feng, T. Qiu, C.-Y. Shen, and X.-Y. Li, Electromagnetic and absorption properties of carbonyl iron/rubber radar absorbing materials, IEEE Trans. Magn. **42**, 363 (2006).

[7] K. Sakai, K. Hiraki, and S. Yoshikado, Evaluation of composite electromagnetic wave absorber made of isolated

Ni-Zn ferrite or permalloy, Electron. Commun. Jpn **92**, 14 (2009).

[8] B. Nam, Y.-H. Choa, S.-T. Oh, S. K. Lee, and K. H. Kim, Broadband rf noise suppression by magnetic nanowire-filled composite films, IEEE Trans. Magn. **45**, 2777 (2009).

[9] A. Makarov, T. Windbacher, V. Sverdlov, and S. Selberherr, CMOS-compatible spintronic devices: A review, Semicond. Sci. Technol. **31**, 113006 (2016).

[10] S. A. Nikitov, D. V. Kalyabin, I. V. Lisenkov, A. N. Slavin, Yu. N. Barabanenkov, S. A. Osokin, A. V. Sadovnikov, E. N. Beginin, M. A. Morozova, Yu. P. Sharaevsky, Yu. A. Filimonov, Yu. V. Khivintsev, S. L. Vysotsky, V. K. Sakharov, and E. S. Pavlov, Magnonics: A new research area in spintronics and spin wave electronics, Physics-Uspekhi **58**, 1002 (2015).

[11] A. V. Chumak, A. A. Serga, and B. Hillebrands, Magnonic crystals for data processing, J. Phys. D: Appl. Phys. **50**, 244001 (2017).

[12] T. Manago, M. M. Aziz, F. Ogrin, and K. Kasahara, Influence of the conductivity on spin wave propagation in a permalloy waveguide, J. Appl. Phys. **126**, 043904 (2019).

[13] A. Aharoni and S. Shtrikman, Magnetization curve of the infinite cylinder, Phys. Rev. **109**, 1522 (1958).

[14] C. Kittel, On the theory of ferromagnetic resonance absorption, Phys. Rev. **73**, 155 (1948).

[15] R. I. Joseph and E. Schlömann, Theory of magnetostatic modes in long, axially magnetized cylinders, J. Appl. Phys. **32**, 1001 (1961).

[16] W. F. Brown, *Micromagnetics, Robert E* (Krieger Publishing Co., New York, 1978).

[17] R. Arias and D. L. Mills, Theory of spin excitations and the microwave response of cylindrical ferromagnetic nanowires, Phys. Rev. B **63**, 134439 (2001).

[18] W. S. Ament and G. T. Rado, Electromagnetic effects of spin wave resonance in ferromagnetic metals, Phys. Rev. **97**, 1558 (1955).

[19] G. T. Rado and J. R. Weertman, Spin-wave resonance in a ferromagnetic metal, J. Phys. Chem. Solids **11**, 315 (1959).

[20] R. E. Camley and D. L. Mills, Theory of microwave propagation in dielectric/magnetic film multilayer structures, J. Appl. Phys. **82**, 3058 (1997).

[21] J. W. Hartwell, Standing spin waves in ferromagnetic thin films, Proc. IEEE **56**, 23 (1968).

[22] B. Heinrich, The theory of ferromagnetic resonance in metal whiskers, Czech. J. Phys. B **17**, 1264 (1967).

[23] L. Kraus, Theory of ferromagnetic resonance in thin wires, Czech. J. Phys. B **32**, 1264 (1982).

[24] L. Kraus, G. Infante, Z. Frait, and M. Vázquez, Ferromagnetic resonance in microwires and nanowires, Phys. Rev. B **83**, 174438 (2011).

[25] R. N. Nosov and D. I. Sementsov, Skin effect under the conditions of ferromagnetic and spin-wave resonance, Phys. Solid State **43**, 1923 (2001).

[26] D. Ménard, M. Britel, P. Ciureanu, and A. Yelon, Giant magnetoimpedance in a cylindrical magnetic conductor, J. Appl. Phys. **84**, 2805 (1998).

[27] C. McKeever, F. Y. Ogrin, and M. M. Aziz, Microwave magnetization dynamics in ferromagnetic spherical nanoshells, Phys. Rev. B **100**, 054425 (2019).

[28] J. Cantu-Valle, I. Betancourt, J. E. Sanchez, F. Ruiz-Zepeda, M. M. Maqableh, F. Mendoza-Santoyo, B. J. H. Stadler, and A. Ponce, Mapping the magnetic and crystal structure in cobalt nanowires, J. Appl. Phys. **118**, 024302 (2015).

[29] A. Taflove and S. C. Hagness, *Computational Electrodynamics: The Finite-Difference Time-Domain Method* (Arctech House, Boston, Mass., 2000), 2nd ed.

[30] Z. Yao, R. U. Tok, T. Itoh, and Y. E. Wang, A multiscale unconditionally stable time-domain (MUST) solver unifying electrodynamics and micromagnetics, IEEE Trans. Microw. Theory Tech. **66**, 2683 (2018).

[31] I. S. Maksymov and M. Kostylev, Impact of conducting nonmagnetic layers on the magnetization dynamics in thin-film magnetic nanostructures, J. Appl. Phys. **113**, 043927 (2013).

[32] I. S. Maksymov and M. Kostylev, Impact of eddy currents on the dispersion relation of surface spin waves in thin conducting magnetic films, J. Phys. D: Appl. Phys. **46**, 495001 (2013).

[33] Z. Yao, H. Cui, and Y. E. Wang, in *IEEE MTT-S International Microwave Symposium (IMS)*, Boston, MA, USA (2019), p. 110.

[34] A. D. Greenwood, D. M. French, B. W. Hoff, and S. L. Heidger, in *28th Annual Review of Progress in Applied Computational Electromagnetics 2012 Conference Proceedings*, 10-14 April 2012, Columbus, Ohio, USA. Volume: Multi-Physics Modeling and Simulations.

[35] A. D. Greenwood, D. M. French, B. W. Hoff, and S. L. Heidger, in *2014 USNC-URSI Radio Science Meeting (Joint with AP-S Symposium)*, Memphis, TN, (2014), pp. 48–48.

[36] J. A. Pereda, L. A. Vielva, A. Vegas, and A. Prieto, A treatment of magnetized ferrites using the FDTD method, IEEE Microw. Guid. Wave Lett. **3**, 136 (1993).

[37] J. A. Pereda, L. A. Vielva, M. A. Solano, A. Vegas, and A. Prieto, FDTD analysis of magnetized ferrites: Application to the calculation of dispersion characteristics of ferrite-loaded waveguides, IEEE Trans. Microw. Theory Tech. **43**, 350 (1995).

[38] G. Zheng and K. Chen, Transient analysis of microstrip lines with ferrite substrate by extended FDTD method, Int. J. Infrared Millimeter Waves **13**, 1115 (1992).

[39] A. T. Reineix and F. Jecko, Ferrite analysis using the finite-difference time-domain (FDTD) method, Microw. Opt. Technol. Lett. **5**, 685 (1992).

[40] M. Okoniewski and E. Okoniewska, FDTD analysis of magnetized ferrites: A more efficient algorithm, IEEE Microw. Guid. Wave Lett. **4**, 169 (1994).

[41] O. Vacus and N. Vukadinovic, Dynamic susceptibility computations for thin magnetic films, J. Comput. Appl. Math. **176**, 263 (2005).

[42] M. M. Aziz, Sub-nanosecond electromagnetic-micromagnetic dynamic simulations using the finite-difference time-domain method, PIER B **15**, 1 (2009).

[43] S. Chikazumi, *Physics of Ferromagnetism* (Oxford University Press, Oxford, 1997), 2nd ed., Chap 3, p. 69.

[44] A. Aharoni, *Introduction to the Theory of Ferromagnetism, Sec. 5* (Oxford University Press, Oxford, 2007), 2nd ed., p. 86.

[45] J. E. Miltat and M. J. Donahue, in *Handbook of Magnetism and Advanced Magnetic Materials*, edited by H. Kronmüller, S. Parkin, J. E. Miltat, M. R. Scheinfein (John Wiley & Sons, New Jersey, 2007).
[46] K. S. Yee, Numerical solution of inital boundary value problems involving Maxwell's equations in isotropic media, IEEE Trans. Ant. Prop. **14**, 302 (1966).
[47] J. B. Schneider, Understanding the Finite-Difference Time-Domain Method, ww.eecs.wsu.edu/∼schneidj/ufdtd (2010).
[48] J. Berenger, A perfectly matched layer for the absorption of electromagnetic waves, J. Comput. Phys. **114**, 185 (1994).
[49] M. Slodicka and I. Cimrak, Numerical study of nonlinear ferromagnetic materials, Appl. Numer. Math. **46**, 95 (2003).
[50] I. Mayergoyz, G. Bertotti, and C. Serpico, *Nonlinear Magnetization Dynamics in Nanosystems, Chap 11* (Elsevier Science, Amsterdam, 2009).
[51] P. K. Tannenwald and R. Weber, Exchange integral in cobalt from spin-wave resonance, Phys. Rev. **121**, 715 (1961).
[52] S. Chikazumi, *Physics of Ferromagnetism, Chap 12* (Oxford University Press, Oxford, 1997), 2nd ed., pp. 249.
[53] A. D. Avery, S. J. Mason, D. Bassett, D. Wesenberg, and B. L. Zink, Thermal and electrical conductivity of approximately 100-nm permalloy, Ni, Co, Al, and Cu films and examination of the wiedemann-franz Law, Phys. Rev. B **92**, 214410 (2015).
[54] A. Thiaville, D. Thomas, and J. Miltat, On corner singularities in micromagnetics, Phys. Stat. Sol. **170**, 125 (1998).
[55] M. Beleggia, M. De Graef, and Y. T. Millev, The equivalent ellipsoid of a magnetized body, J. Phys. D: Appl. Phys. **39**, 891 (2006).
[56] A. Aharoni, Demagnetizing factors for rectangular ferromagnetic prisms, J. Appl. Phys. **83**, 3432 (1998).
[57] A. G. Gurevich and G. A. Melkov, *Magnetization Oscillations and Waves* (CRC Press, Boca Raton, 1996), p. 189, Section 7.2.2.
[58] C. Kittel, Excitation of spin waves in a ferromagnet by a uniform rf field, Phys. Rev. **110**, 1295 (1958).
[59] K. Y. Guslienko and A. N. Slavin, Boundary conditions for magnetization in magnetic nanoelements, Phys. Rev. B **72**, 014463 (2005).
[60] K. Y. Guslienko, R. W. Chantrell, and A. N. Slavin, Dipolar localization of quantized spin-wave modes in thin rectangular magnetic element, Phys. Rev. B **68**, 024422 (2003).
[61] G. Gubbiotti, M. Conti, G. Carlotti, P. Candeloro, E. Di Fabrizio, K. Y. Guslienko, A. Andre, C. Bayer, and A. N. Slavin, Magnetic field dependence of quantized and localized spin wave modes in thin rectangular magnetic dots, J. Phys.: Condens. Matter **16**, 7709 (2004).
[62] R. I. Joseph and E. Schlömann, Demagnetizing field in nonellipsoidal bodies, J. Appl. Phys. **36**, 1579 (1965).
[63] A. Smith, K. K. Nielsen, D. V. Christensen, C. R. H. Bahl, R. Bjørk, and J. Hattel, The demagnetizing field of a nonuniform rectangular prism, J. Appl. Phys. **107**, 103910 (2010).
[64] J. D. Jackson, *Classical Electrodynamics, Chap 6* (John Wiley & Sons Inc, New York, 1999), 3rd ed., p. 258.
[65] R. F. Soohoo, *Microwave Magnetics* (Harper & Row Publishers, New York, 1985).